Article

Effect of Alkali and Trivalent Metal Ions on the High-Pressure Phase Transition of $[C_2H_5NH_3]M^I_{0.5}M^{III}_{0.5}(HCOO)_3$ (M^I = Na, K and M^{III} = Cr, Al) Heterometallic Perovskites

Maciej Ptak,* Katrine L. Svane, Ines E. Collings, and Waldeci Paraguassu

Read Online

ACCESS | Metrics & More | Article Recommendations | SI Supporting Information

ABSTRACT: We report the high-pressure behavior of two perovskite-like metal formate frameworks with the ethylammonium cation (EtAKCr and EtANaAl) and compare them to previously reported data for EtANaCr. High-pressure single-crystal X-ray diffraction and Raman data for EtAKCr show the occurrence of two high-pressure phase transitions observed at 0.75(16) and 2.4(2) GPa. The first phase transition involves strong compression and distortion of the KO_6 subnetwork followed by rearrangement of the $-CH_2CH_3$ groups from the ethylammonium cations, while the second involves octahedral tilting to further reduce pore volume, accompanied by further configurational changes of the alkyl chains. Both transitions retain the ambient $P2_1/n$ symmetry. We also correlate and discuss the influence of structural properties (distortion parameters, bulk modulus, tolerance factors, and compressibility) and parameters calculated by using density functional theory (vibrational entropy, site-projected phonon density of states, and hydrogen bonding energy) on the occurrence and properties of structural phase transitions observed in this class of metal formates.
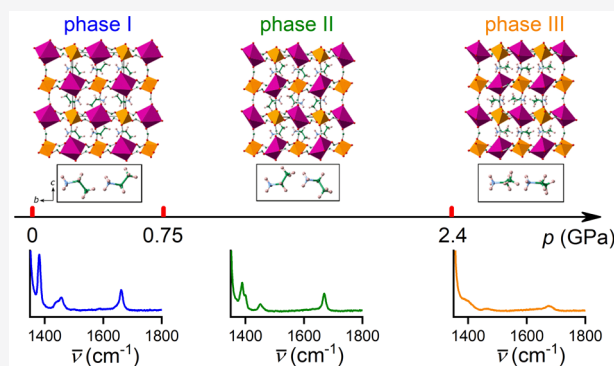
INTRODUCTION

The broad interest in dense formate-based metal−organic frameworks (MOFs) began when Jain et al. reported just over 10 years ago multiferroic properties of the $[(CH_3)_2NH_2]Mn(HCOO)_3$ compound adopting perovskite-like architecture.[1] Since then, there have been a lot of reports that show the unique properties among this class of compounds, that is, ferroelectricity, ferroelasticity, luminescence, dielectric, magnetic, vibrational, mechanical, spectroscopic, and luminescence properties.[2−8] Because the multifunctional properties of MOFs can be easily tuned by substitution of metal ions, linkers, and protonated amines, a few subgroups have been formed, that is, the M^{II}-based perovskite-type structures,[1,2,4−7,9,10] the chiral structures,[9−11] heterometallic niccolite-type structures (with the $M^{II}−M^{III}$ mixture),[12,13] or heterometallic alkali ion composed compounds with the general formula $[A]M^I_{0.5}M^{III}_{0.5}(HCOO)_3$ (A = protonated amine, M^I = Na^+, K^+, and M^{III} = Al^{3+}, Cr^{3+}, Fe^{3+}). The last group is a small subclass of formate MOFs that have attracted a lot of attention due to their unique structure-related properties depending on the applied building blocks, that is, luminescence, ferroelectricity, or ferroelasticity.[14−20] Ferroic properties are related to the order−disorder phase transitions that can be precisely controlled by temperature. Among the studied heterometallic MOFs with different protonated amines (ammonia, Am^+; imidazole, Im^+; dimethylamine, DMA^+; ethylamine, EtA^+;

methylamine, MeA^+, etc.),[14,16−18,20−23] only a few exhibit structural ordering. Three analogues with the EtA^+ cation and Na^+ ions, $EtANa_{0.5}M^{III}_{0.5}(HCOO)_3$ (M^{III} = Al^{3+}, Cr^{3+}, Fe^{3+}), adopt monoclinic polar Pn symmetry with ordered EtA^+ cations in two independent sites (Figure 1a).[14,16,20,23] Although it has not been confirmed experimentally, the density functional theory (DFT) calculations showed that EtANaFe and EtANaCr could be considered as ferroelectrics with the polarization estimated to (0.2, 0, 0.8) μCcm^{-2} and (0.3, 0, 0.9) μCcm^{-2}, respectively.[14,20] Increasing the temperature to 360−373 K (depending on the trivalent cation) leads to a structural phase transition to another monoclinic symmetry ($P2_1/n$) with disordered EtA^+ cations and a loss of ferroic properties (Figure 1c).[14,23] The increase of pressure up to 3.6 GPa, however, causes an enhancement of the spontaneous polarization in the Pn phase of EtANaCr.[20]

The substitution of Na^+ ions by larger K^+ ions changes the properties of the MOF dramatically; that is, the polar Pn phase is suppressed, and at room temperature (RT) the EtAKCr
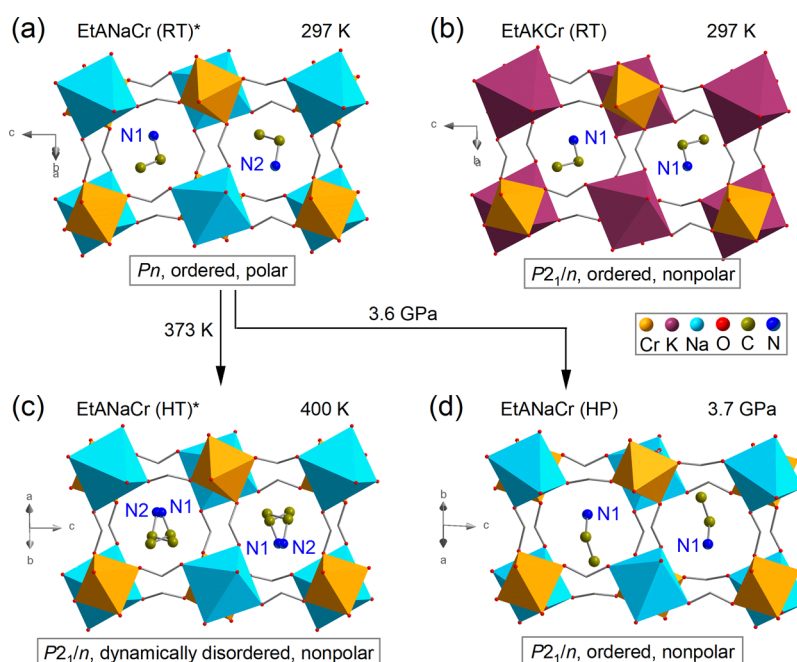
Figure 1. Ambient (a), HT (c), and HP (d) phases of EtANaCr together with ambient phase of EtAKCr (b). Phases of EtANaCr indicated by asterisks are isomorphic for EtANaAl and EtANaFe. The H atoms are omitted for clarity.

crystal adopts the high-temperature (HT) nonpolar phase of $EtANa_{0.5}M^{III}_{0.5}(HCOO)_3$ but with ordered EtA^+ cations (Figure 1b).[16] It was suggested that the suppression results from the higher flexibility of the framework composed of K^+ and Cr^{3+} metal ions and the larger size of the voids accommodating the EtA^+ cations.[16]

The behavior observed for analogues with the DMA^+ cation is different. The DMANaCr, DMANaFe, and DMAKCr crystals all adopt the trigonal $R\bar{3}$ symmetry with the DMA^+ cations dynamically disordered over three equivalent positions.[15−17] DMANaCr does not undergo any phase transition upon cooling; however, the DMA^+ cations slow down and finally freeze statistically in one of three equivalent positions around the trigonal axis.[17] The substitution of Cr^{3+} ions by Fe^{3+} changes the properties such that an order−disorder phase transition to a triclinic $P\bar{1}$ symmetry with completely ordered DMA^+ cations occurs at 167 K.[15] Substituting the alkali ions does not suppress the occurrence of the phase transition, and the DMAKCr crystal transforms at 190 K to the triclinic $P\bar{1}$ symmetry; however, the arrangement of DMA^+ cations is different from that observed for DMANaFe. In the low-temperature (LT) phase of DMAKCr, the DMA^+ cations remain disordered, but the HT dynamical disorder transforms to a 2-fold statistical type of disorder.[16]

Herein we report the high-pressure studies of EtAKCr and EtANaAl to understand the structural properties under different external stimuli. In our previous work, we have shown that many heterometallic MOFs exhibit one or two phase transitions under hydrostatic compression.[18,20] Raman spectra showed that DMANaCr transforms to another symmetry phase at 4.0−4.4 GPa, and the substitution of Na^+ ions with K^+ ions leads to a decrease in the transition pressure to 2.0−2.5 GPa.[18] Our latest studies of EtANaCr showed that it undergoes a structural transformation at 3.6(2) GPa with loss of polar properties.[20] Using a combination of single-crystal X-ray diffraction and Raman spectroscopy at high pressure, the mechanism of this first-order phase transition could be

described. It mainly involves the compression of NaO_6 units along the b-direction and is accompanied by reorientation of the EtA^+ cations in the shrinking voids.[20]

In this article we gain further insight into the influence of the alkali and trivalent metal cations on the structural properties affecting the high-pressure phase transitions by performing high-pressure experiments on the EtAKCr and EtANaAl analogues. The main goal of this work is to define and understand how high pressure influences the flexible framework of EtAKCr and the orientation of organic cations accommodated in the voids. Because reported temperature-dependent properties of EtANaCr and EtAKCr are completely different, we aim to understand the mechanisms and crucial factors determining the type of transition, if any, that could occur under high-pressure stimuli. Therefore, we perform high-pressure single-crystal X-ray diffraction (XRD) studies combined with Raman spectroscopy for EtAKCr. We also perform high-pressure Raman measurements for EtANaAl, which has very similar temperature-dependent properties to EtANaCr, to investigate how the substitution of the M^{III} cation influences the high-pressure behavior. Both techniques have previously been employed for the studies of many formate-based MOFs.[11,20,24−36] Nevertheless, their combination allows the examination of long-range crystalline order together with very subtle local symmetry changes at the same time. DFT calculations are employed to obtain information about the energy of the hydrogen bonds (HBs) and to describe changes related to the HBs during the experiment. Furthermore, the magnitude of the vibrational entropy is calculated to understand how the structural dynamics affects the reorientational motions of the EtA^+ cation within the cage. Calculations for the previously studied EtANaCr[20] are included for comparison.

■ EXPERIMENTAL SECTION

Materials and Instrumentation. All reagents (analytically grade) used for synthesis were commercially available and were
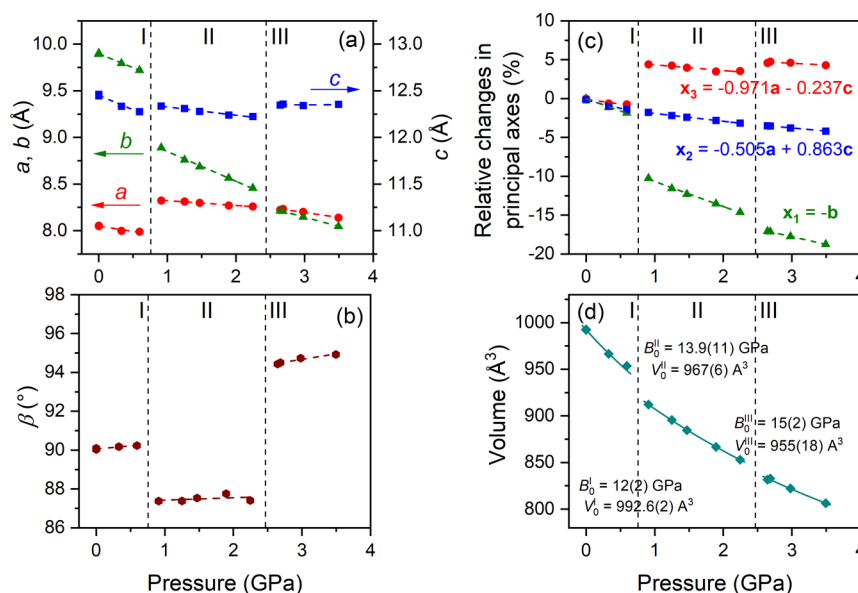
Figure 2. Changes in the lattice a, b, and c parameters (a), monoclinic β angle (b), relative changes in the principal axes (c), and volume (d) with increasing pressure. The x_1 (green triangles), x_2 (blue squares), and x_3 (red circles) were calculated by using PASCal.[45] The volume vs pressure functions were fitted by using a second-order Birch−Murnaghan equation-of-state and are presented in (d) as solid lines (EoSFit[46]). The vertical dashed lines indicate the pressures of the structural phase transitions.

used without further purification. The ambient powder XRD patterns were obtained on an X'Pert PRO X-ray diffraction system equipped with a PIXcel ultrafast line detector, focusing mirror, and Soller slits for Cu Kα radiation (λ = 1.54056 Å).

Synthesis of the Samples. The EtAKCr and EtANaAl crystals were synthesized by using a hydrothermal technique described previously.[16,23] The phase purity of both bulk samples was confirmed by the good match of their powder XRD patterns with a simulation from the single-crystal structural data for Cu Kα radiation (λ = 1.54056 Å) (Figure S1, Supporting Information) taken from crystal information file (CIF) available in the literature.[16,19,23]

High-Pressure Diffraction. High-pressure single-crystal X-ray diffraction on the EtAKCr formate was measured at the ID15B beamline of the European Synchrotron Radiation Facility, Grenoble, up to 4 GPa using monochromatic X-ray radiation (λ = 0.411189 Å). Membrane driven LeToullec-type diamond anvil cells were used, equipped with Boehler-Almax anvils. Stainless steel was used as the gasket material, and Ne was loaded as the pressure-transmitting medium (ptm). Diffraction patterns were collected with a Mar555 flat-panel detector using steps of 0.5° oscillations over a total ω scan range of 76° about the vertical axis. The pressures were measured by using the ruby fluorescence method before and after each diffraction measurement. The average of both pressure values was used, and the variance was employed to estimate the errors associated with the pressure measurement, in addition to the ±0.05 error to account for the error in the ruby florescence method in the pressure range below 4 GPa. Lattice parameter determination and integration of the reflection intensities were performed by using the CrysAlisPro software.[37] Three crystals were selected and positioned in the gasket chamber to increase the likelihood of solving potential high-pressure phases. A small piece of tungsten was also loaded alongside the crystals for centering purposes.

High-Pressure Raman. The high-pressure Raman spectra were recorded in backscattering geometry by using a

microscope attached to a triple-grating spectrometer (Jobin-Yvon T64000). The 514.5 nm line of a solid-state ion laser was used as excitation, and the spectral resolution was 2 cm^{-1}. To reach high pressures, a diamond anvil cell Diacell μScopeDAC-RT(G) from Almax easyLab with a diamond of 0.4 mm of culets was used. The sample was loaded into a 100 μm hole drilled in a stainless steel gasket with a thickness of 200 μm by using an electric discharge machine from Almax easyLab. The nujol (mineral oil) served as the ptm. Pressures were measured based on the shifts of the ruby R$_1$ and R$_2$ fluorescence lines.

Quantum Chemical Calculations. Density functional theory (DFT) calculations were performed by using the Vienna *ab initio* simulation package (VASP)[38] with PAW pseudopotentials and an energy cutoff of 700 eV. The PBEsol functional[39] was used with the D3 correction[40,41] added to account for dispersive interactions. The atomic positions and unit cell dimensions were relaxed until all forces are below 0.01 eV/Å. All of the structures investigated here contain four cations in the unit cell, and the reciprocal space is sampled with a 2 × 2 × 2 k-point mesh.

For structures containing Cr^{3+} ions the calculations were spin-polarized. Previous tests have revealed an energy difference of <1 meV between ferromagnetic and antiferromagnetic ordering of the Cr^{3+} ions in DMAKCr, suggesting a very weak coupling between the spins, which in the EtA$^+$ compounds are located >7.8 Å apart. We therefore chose to optimize the EtANaCr and EtAKCr structures with ferromagnetic alignment of the spins on the Cr^{3+} ions.

Phonopy[42] was used to calculate the vibrational entropy as a function of temperature on a 5 × 5 × 5 q-point mesh. The site-projected phonon density of states, which can be used to obtain the site-projected vibrational entropy, was calculated as previously described.[43]

The HB energy was calculated following the procedure described previously.[44] The total electrostatic interaction between a cation and the cage was calculated as the energy required to remove one cation from the unit cell, and the
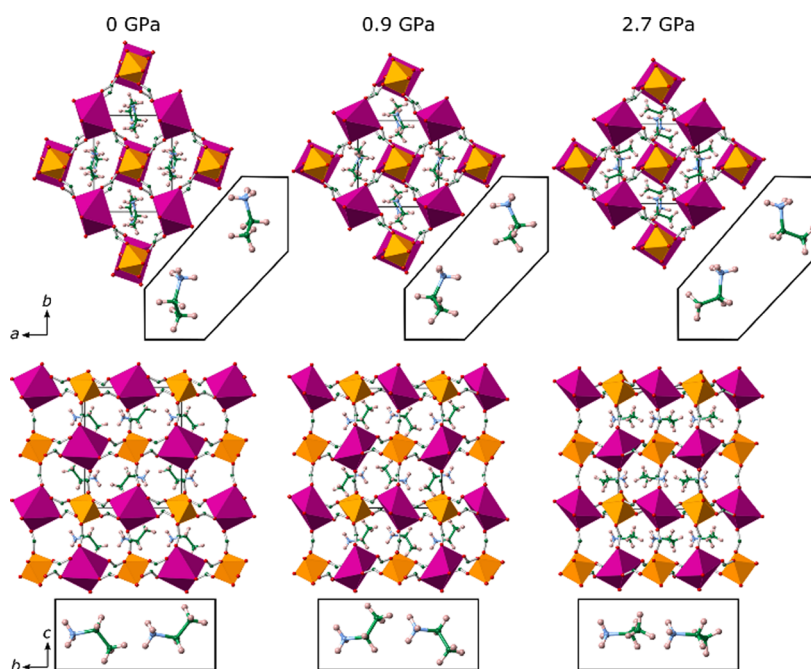
Figure 3. Structures of EtAKCr in each phase (I, II, and III) upon compression, viewed along two different directions. The colored polyhedral represent CrO_6 in orange and KO_6 in purple. The atoms are colored as blue for N, green for C, red for O, and pink for H. The black boxes highlight the orientations of the EtA^+ cations.

dominating monopole term was estimated as the energy required to remove a single atom cation (here Cs^+) from the same cage. Subtracting the monopole part of the electrostatic interaction from the total electrostatic interactions, the dipole and higher order terms remain. These are assumed to be dominated by HBs. We note that the computational setup described here is the same as was used in previous works,[18,44] and the calculated HB energies should therefore be directly comparable.

■ RESULTS AND DISCUSSION

High-Pressure Single-Crystal X-ray Diffraction. The high-pressure diffraction experiment was performed for the EtAKCr crystal. Its ambient pressure phase (phase I) has previously been refined in the monoclinic $P2_1/n$ (no. 14) symmetry with the crystal lattice parameters $a = 8.0147(2)$ Å, $b = 9.8547(3)$ Å, $c = 12.3886(3)$ Å, and $\beta = 90.052(8)°$.[16]

The pressure dependence of the unit cell parameters in the 0−4 GPa range is presented in Figure 2 and Figure S2. They exhibit an abrupt discontinuity in the 0.6−0.9 GPa pressure range, suggesting a first-order phase transition to phase II. This first transition gives rise to an overall unit cell volume decrease of 2.3%. A more subtle distortion to phase III is observed in the 2.2−2.6 GPa range, with no volume discontinuity associated with the transition.

To understand the anisotropy of the unit cell compression, we calculated the pressure dependencies of the principal axes using the PASCal (Principal Axis Strain Calculations) program.[45] The resulting principal axes x_1, x_2, and x_3 are related to the lattice parameters by the following relations: $x_1 = -b$, $x_2 = -0.505a + 0.863c$, and $x_3 = -0.971a - 0.237c$. There is some anisotropy in the compressibility (κ) of the principal axes, as $x_1 > x_2 > x_3$, with x_1 reaching up to about 2% compression (unit cell compression is at ca. 4%) before the first phase transition. The compressibility coefficients κ_1, κ_2, and κ_3 (along the x_1, x_2, and x_3 principal axes, respectively) for

the ambient phase are 31.0(5), 24.4(13), and 12.0(2) TPa^{-1}, respectively. All of them are positive; therefore, the EtAKCr crystal exhibits a typical positive linear compressibility in each principal axis direction. The compressibilities are much larger than for the previously studied EtANaCr crystal ($\kappa_1 = 18.4(1)$ TPa^{-1}, $\kappa_2 = 12.0(2)$ TPa^{-1}, and $\kappa_3 = 3.4(2)$ TPa^{-1}),[20] indicating that EtAKCr is more compressible than its sodium analogue. This can be understood by the larger cation size of K^+ compared to Na^+ (1.38 vs 1.02 Å),[47] which is also manifested in the volume differences known at ambient conditions (978.48(5) vs 904.24(2) $Å^3$).[20,23] Similarly to EtANaCr, the anisotropy in the unit cell compressibility arises from the directionality of the HBs interaction from the EtA^+ cations to the oxygen atoms of the formate linkers (Figure S3), which are mainly located within the ac-plane, making the b-axis (x_1 direction) most compressible.

The unit cell volume vs pressure data were fitted by using the second-order Birch−Murnaghan equation-of-state in each phase using EoSFit[46] (Figure 2d). The fitting yields bulk moduli (B_0) 12(2), 13.9(11), and 15(2) GPa as well as the reference volumes (V_0) 992.6(2), 967(6), and 955(18) $Å^3$ for phases I, II, and III, respectively. These values are much lower than the B_0 values obtained for EtANaCr (20.1(2) and 23.3(17) GPa for phases I and II),[20] thus classifying the EtAKCr crystal as much softer than EtANaCr. The replacement of Na^+ ions by larger K^+ ions not only gives a more compressible material but also leads to a lowering of the phase transition pressure as well as an additional transition. The reduction in phase transition pressure due to changes in the metal cations with larger radii is also observed for DMANaCr and DMAKCr (by ∼2 GPa)[18] as well as for $DMAM^{II}$ (M^{II} = Mn, Fe)[36] and ammonium metal formates (M^{II} = Mn, Ni, Fe, Zn).[24,25]

The refined crystal structures within the three phases (ambient phase I, phase II, and phase III) are given in Figure 3. Both high-pressure phase transitions did not show any
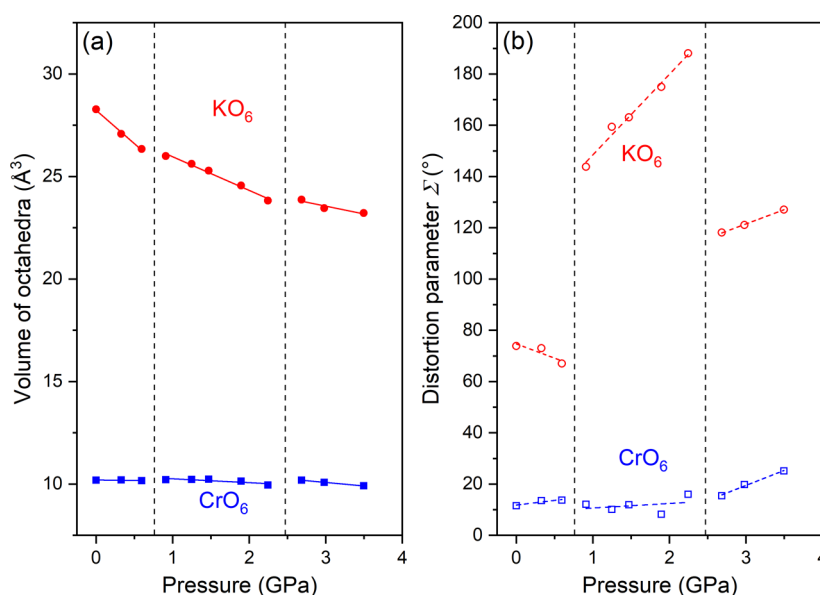
Figure 4. KO_6 and CrO_6 volume (a) and angle distortion parameter Σ (b) as a function of pressure. The dashed vertical lines represent the pressures, where the structural phase transitions take place.
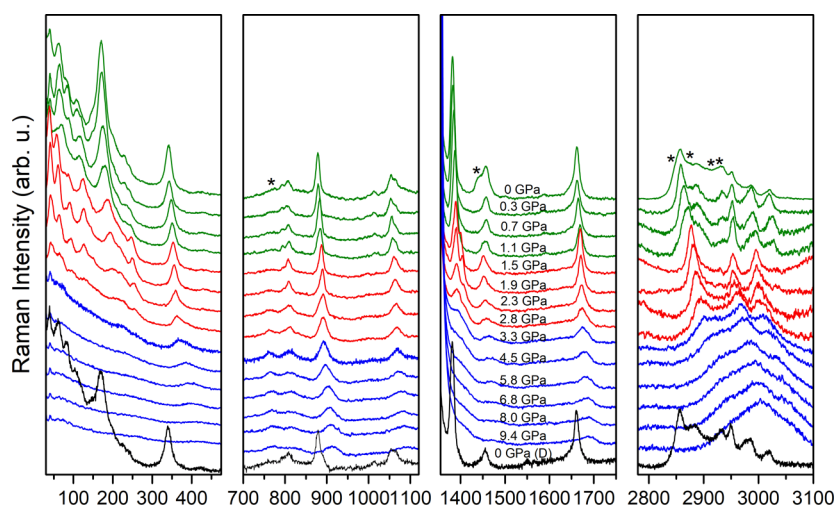

Figure 5. Pressure evolution of Raman spectra for the EtAKCr crystal in phase I (green color), II (red color), and III (blue color); stars denote bands originating from the ptm.

evidence of a change in monoclinic symmetry, and the same centrosymmetric $P2_1/n$ space group as found at ambient conditions could be used to refine both high-pressure phases (Table S1). At the first phase transition, a large compression of the KO_6 octahedra can be observed along the *b*-axis, where there are no NH···O HBs. This results in an abrupt increase in octahedral distortion for the KO_6 octahedra, as illustrated by the change in distortion angle parameter plotted in Figure 4 (a comparison with EtANaCr is presented in Figure S4). The distortion angle parameter Σ is defined as $\sum_{i=1}^{12}(|\varphi_i - 90|)$, where φ_i denotes the 12 *cis* angles in the octahedral coordination sphere,[17,48] and a large value thus indicates a large deviation from perfect octahedral geometry. The framework compression also results in a reorientation of the $-CH_2CH_3$ groups from the EtA^+ cations to pack more efficiently along the *b*-axis. Upon further compression, a second transition takes place, which involves both KO_6 and CrO_6 octahedral rotations to reduce pore space even further. At this transition, the configuration of the EtA^+ cations is also

affected such that the structure can be optimally compressed along the *b*- and *c*-axes, and changes to a different arrangement, similar to that observed in the high-pressure phase of EtANaCr, (Figure 4). The position of the $-NH_3$ group of the EtA^+ cation is maintained across all transitions, highlighting its strong interaction with the metal formate framework through hydrogen bonding interactions. The methylene and methyl groups from the EtA^+ cation are, in contrast, very mobile and change configuration to optimize pore space requirements as the framework is compressed.

High-Pressure Raman Scattering. The high-pressure Raman experiments were performed for the EtAKCr and EtANaAl crystals to better understand the influence of both the alkali and trivalent transition metal ions on the structural properties under compression. Figure 5 presents Raman spectra of the EtAKCr crystal measured up to 9.4 GPa. The evolution of the observed bands is presented in Figure 6. The spectrum at ambient pressure is nearly identical to the spectrum obtained outside the pressure chamber;[16] however,
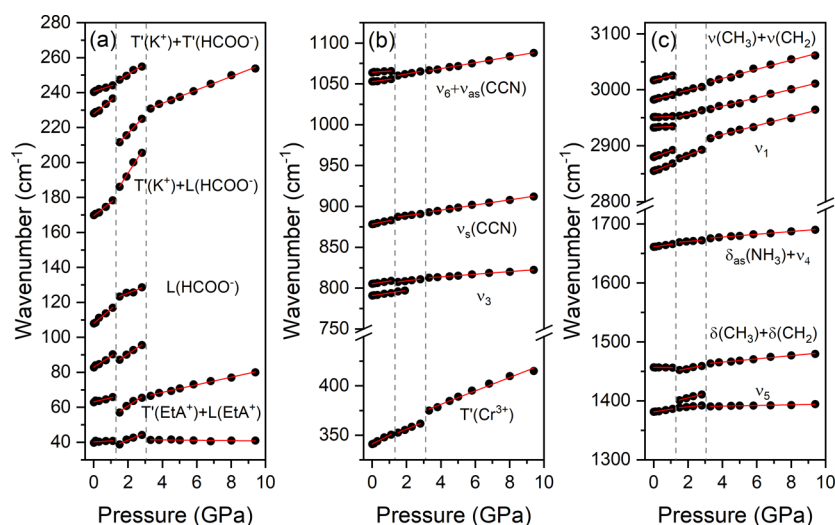
Figure 6. Pressure dependence of Raman wavenumbers for EtAKCr. The vertical lines represent the pressures where the structural phase transitions take place. The ν, ν_s, ν_{as}, δ, δ_{as}, ν_1, ν_3, ν_4, ν_5, ν_6, T′, and L symbols denote stretching, symmetric stretching, antisymmetric stretching, bending, antisymmetric bending, the CH stretching, the symmetric OCO bending, the antisymmetric CO stretching, the CH in-plane bending, the CH out-of-plane bending, translational, and librational mode, respectively.
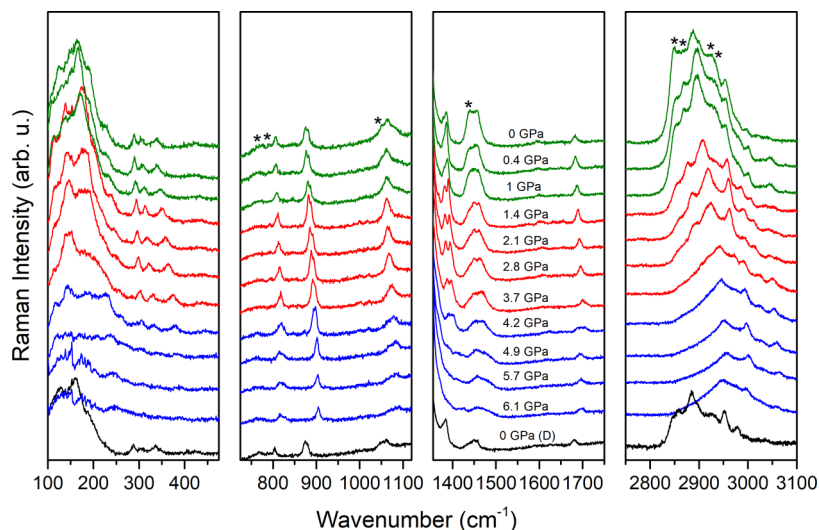

Figure 7. Pressure evolution of Raman spectra for the EtANaAl crystal in phase I (green color), II (red color), and III (blue color); stars denote bands originating from the ptm.

some additional bands are observed due to the ptm. The spectrum remains quantitatively unchanged up to 1.1 GPa. At 1.5 GPa some bands split or disappear, the abrupt character suggesting that this is most likely a first-order phase transition. A further increase in pressure causes another clear feature that can be attributed to a second phase transition in the 2.3−2.8 GPa pressure range. The pressures of these transitions are in a good agreement with the phase transition pressures observed in the high-pressure XRD experiment.

To understand how the changes of modes reflect the structural features, we fit their pressure dependence to the linear $\omega(P) = \omega_0 + \alpha P$ function. The ω_0 and α coefficients describe the interception at zero-pressure and the slope of the curve ($\alpha = d\omega/dP$), respectively. The results of fitting are presented in Figure 6. Table S2 lists obtained parameters together with proposed assignment of modes based on previous works.[16]

In phase I the highest values of the α coefficients are observed for the lattice modes (6.40−8.93 cm^{-1} GPa^{-1}) and the modes corresponding to the stretching of CH bonds of the EtA$^+$ cations (7.56−8.03 cm^{-1} GPa^{-1}) and formate ions (11.00−12.09 cm^{-1} GPa^{-1}). The high values of the α coefficients for modes corresponding to translational motions of K$^+$ ions arranged in highly ionic KO$_6$ octahedra prove their strong shrinking (Figure 4) and tilting. The Cr−O bonds are significantly stiffer than the K−O bonds, making them very sensitive to even very small structural changes (including distortion or tilting); therefore, observed high values of the α coefficients of Cr^{3+} translations are not associated with a significant volume change of the CrO$_6$ octahedra.

The modes of the carboxyl groups have moderate (2.74−4.41 cm^{-1} GPa^{-1}) values. It suggests that the compression of phase I mainly involves changes in the metal formate framework and in the dynamics of the CH bonds that cannot be easily detected by using XRD methods. The low to
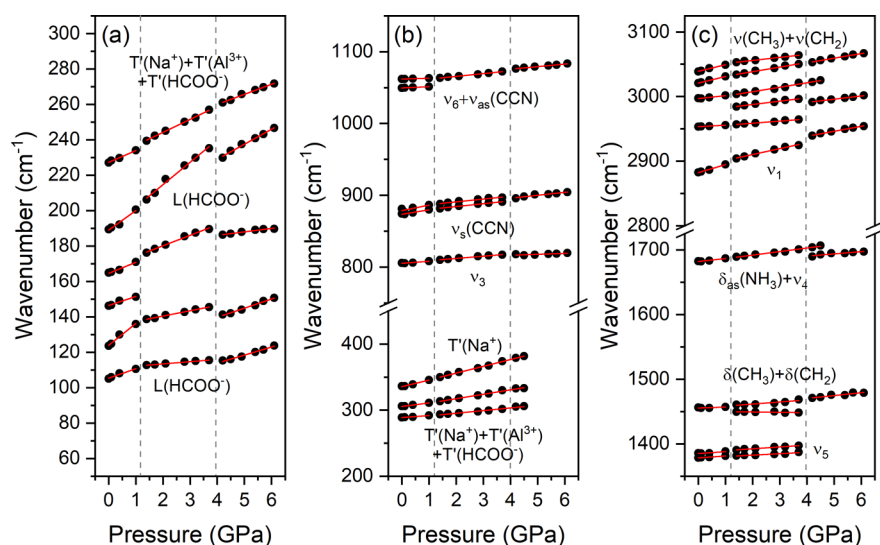
Figure 8. Pressure dependence of Raman wavenumbers for EtANaAl. The vertical lines represent the pressures, where the structural phase transitions take place. The ν, ν_s, ν_{as}, δ, δ_{as}, ν_1, ν_3, ν_4, ν_5, ν_6, T', and L symbols denote stretching, symmetric stretching, antisymmetric stretching, bending, antisymmetric bending, the CH stretching, the symmetric OCO bending, the antisymmetric CO stretching, the CH in-plane bending, the CH out-of-plane bending, translational, and librational mode, respectively.

moderate values associated with other modes of the EtA$^+$ cations suggest that they are less affected.

The further changes of the α coefficients during compression in phase II show that the CH bonds are still strongly influenced. The stretching modes have nearly the same values as observed in phase I, but the bending modes exhibit larger values. An increase in the α factors is also observed for modes assigned to the vibrations of the CCN skeleton of the EtA$^+$ cation, suggesting that the dynamics of the cation is different in phases I and II. A strong increase for the lattice modes, especially for those with contributions from the K$^+$ ions, is observed (up to 15.37 cm^{-1} GPa^{-1} for mode no 20). This behavior clearly corresponds to strong increase of their distortion evidenced by XRD experiment. Therefore, the metal formate framework is further strongly deformed and compressed in phase II. The second phase transition leads to the disappearance of many lattice modes (see Figures 5 and 6). The remaining ones have much lower values of the α coefficients in comparison with phase II. The value obtained for the translational mode of the Cr^{3+} ions is still as high as it was in phases I and II. The lack of a clear jump in the α coefficients is a further proof that the CrO$_6$ sublattice is not subjected to shrinking and/or deformation. Indeed, the volume of the CrO$_6$ octahedra is largely unchanged as can be seen from Figure 3. The high values of α for bands corresponding to CH stretching modes suggest that in this phase the dynamics of the EtA$^+$ cations within the voids are also affected.

In contrast to the EtANaCr crystal, EtAKCr does not show any sign of amorphization even at pressures up to 9.4 GPa. The spectrum after decompression is nearly identical to the one measured before compression (Figure 5). In the case of EtANaCr studied previously, partial amorphization was suggested since the spectrum after decompression was not fully recovered despite the experiment being performed up to 6.2 GPa only.[20]

The EtANaAl crystal is expected to have similar pressure-dependent properties to EtANaCr since their structural and temperature-dependent properties are very similar. Additionally, the ionic radii of Cr^{3+} (61.5 pm)[47] and Al^{3+} (53.5 pm)[47]

and their electronegativity are comparable (1.6 and 1.5, respectively). Figure 7 shows Raman spectra of EtANaAl up to 6.1 GPa, Figure 8 presents the pressure-dependent evolution of the observed Raman modes, and Table S3 lists the results of fitting and the assignment of the observed Raman modes. Surprisingly, EtANaAl exhibits two pressure-induced phase transitions, while only one was observed for the EtANaCr crystal.[20] The ambient-pressure phase (phase I) transforms between 1.0 and 1.4 GPa to phase II and further to phase III when the pressure reaches 4.2 GPa. The compression of phase I shows large α coefficients for lattice modes, especially those assigned to formate ions and translational motions of the Na$^+$ ions, which suggests that the metal formate framework is affected during the compression. On the basis of our previous high-pressure experiments, one can expect that such deformation involves strong shrinking of the NaO$_6$ octahedra and their tilting with simultaneous slight changes in the AlO$_6$ sublattice.[20] In this case we have also noticed large coefficients for the CH stretching modes and modes attributed to the vibrational motions of the CCN skeleton of the cation. In phase II, all large α coefficients are decreased, suggesting that the effect of pressure on the EtA$^+$ cations in this phase is weaker. The value of α for mode no. 17, which has the strongest contribution from translational motions of the Na$^+$ ions, is nearly the same (10.27 cm^{-1} GPa^{-1}), reflecting further distortion of the metal formate framework. The increased coefficient for mode no. 7 assigned to the antisymmetric CO stretching and NH$_3^+$ deformation suggests that the HBs are also affected in this phase, and possibly a reorganization takes place. When the pressure reaches 4.2 GPa, some of the modes disappear. The CH stretching and skeleton CCN vibrations seem to be similarly affected in phases II and III, while the majority of lattice modes have lower pressure coefficients, reflecting that the compression of the metal formate framework is suppressed in this phase. A similar effect was observed for the phase II of EtANaCr which exists at pressures above 4.4 GPa.[20] This could indicate that the transition observed for the EtANaCr crystal is closely related to the transition between phases II and III for EtANaAl. The spectrum of EtANaAl is

fully recovered after releasing 6.1 GPa pressure, suggesting that EtANaAl is more stable than EtANaCr, which experienced partial amorphization above 6.2 GPa.[20]

DFT Calculations of Hydrogen Bonding Strength and Vibrational Entropy. Structural optimization of EtANaCr, EtAKCr, and EtANaAl was performed by using DFT calculations. The optimized unit cell parameters of all three compounds are found to be in reasonable agreement with the experimental values as shown in Table S4. In our previous study of EtANaCr we showed that the crystal was easiest to compress along the b-axis, which is the direction along the length of the EtA$^+$ cations and perpendicular to the plane of the HBs.[20] Calculations of EtANaAl at reduced volume shows that EtANaAl shrinks mostly along the b-axis, in agreement with the diffraction experiments on EtANaCr and EtAKCr that show the largest compressibility in this direction. This is the direction perpendicular to the plane of the HBs, suggesting that hydrogen bonding enhances the mechanical strength of the frameworks along their length.

To further investigate the influence of HBs, we calculated the HB energy of EtANaAl, EtAKCr, and EtANaCr following the procedure described previously.[44] The results listed in Table 1 show that the HB energies are in the range 0.83–0.99

Table 1. Total hydrogen bonding energies (E_{tot}) and the HB energies per N–H bond (E_{NH}) for the EtA$^+$-based formate perovskites along with their transition temperatures (T_c), the volume per cation (V/cation), and the tolerance factor (TF) calculated as described previously[49]

	EtANaCr	EtANaAl	EtAKCr
E_{tot} (eV)	0.94	0.83	0.99
E_{NH} (eV)	0.31	0.28	0.33
T_c (K)	373[23]	369[16]	
V/cation (Å^3)	214	211	237
TF	0.95	0.92	0.90

eV, which is stronger than calculated values for DMA$^+$ frameworks but weaker than the values calculated for hydrazinium (Hyd$^+$) and guanidinium (Gua$^+$) in the Zn^{2+}-based frameworks.[18,44] The DMA$^+$ cation has two N–H bonds per molecule while EtA$^+$ has 3, Hyd$^+$ has 5, and Gua$^+$ has 6, and it is found that the energy per N–H group (E_{NH}) is comparable for all compounds with a given metal. For the EtA$^+$ compounds with different metals the hydrogen bonding strengths follow the order EtAKCr > EtANaCr > EtANaAl. This is similar to previous results for the DMA$^+$ cation, which showed the order DMAKCr > DMANaCr > DMAZn.[18] To our knowledge, the synthesis of EtAZn has not been reported, but assuming that it crystallizes in the same space group as the Mn compound ($Pna2_1$),[50] the HB energy is indeed calculated to be lower than for the three mixed metal compounds (0.66 eV, cf. Table S4). In ref 9 the higher HB strength in the mixed metal formates was explained by the low electronegativity of the alkali metal, which leads to a more ionic metal–oxygen bond and thereby a more negative partial charge on the oxygen atoms of the NaO$_6$ or KO$_6$ octahedra.[18] The idea that this leads to stronger HBs is further supported by the observation that the cations in all the EtA$^+$ compounds form more HBs with the oxygen atoms of the NaO$_6$ and KO$_6$ octahedra than with the oxygen atoms of the AlO$_6$ or CrO$_6$ octahedra.

Interestingly, although the EtANaCr and EtANaAl compounds have similar hydrogen bonding parameters (cf. Table

S5) and transition temperatures, the hydrogen bonding energy is somewhat different. To further compare these two compounds, we consider the flexibility of the metal formate cage, characterized by the phonon density of states (Pdos) and the resulting vibrational entropy (S_{vib}). This factor has previously been shown to have an important influence on the occurrence of phase transitions with changes in temperature or pressure.[18,51,52] The phonon frequencies depend on the relative magnitude of the force constant of the bonds and the reduced mass of the involved atoms, and modes with low frequencies will give the largest contributions to the vibrational entropy. The reduced mass of the metal formate cages of the EtA$^+$ compounds increases following the series EtANaAl < EtANaCr < EtAKCr, which would lead to an expected ordering of the frequencies EtAKCr < EtANaCr < EtANaAl; however, the shorter and more covalent Al–O and Cr–O bonds are expected to have larger force constants and therefore also higher frequencies than the other bonds. This can indeed be seen in Figure 9, which shows the phonon density of states
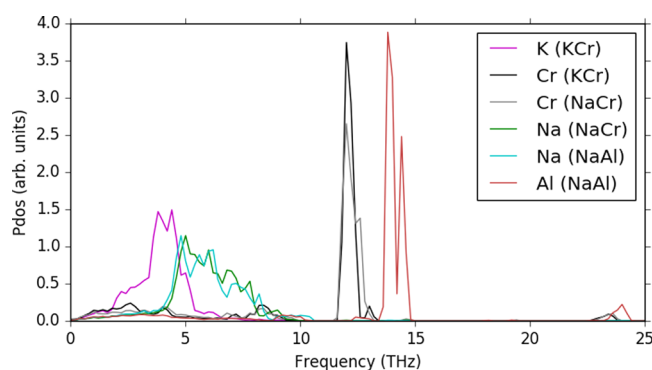

Figure 9. Phonon density of states projected on the metal atoms of the EtA$^+$ frameworks. The graphs are normalized by the number of atoms of that type.

projected on the metal sites for the four different compounds. The modes associated with Cr^{3+} and Al^{3+} are found at higher frequencies than those associated with Na$^+$, while modes associated with K$^+$ are found at very low frequencies.

The overall effect on the vibrational entropy can be seen in Figure 10. The EtAKCr compound has the highest vibrational entropy at all temperatures while the EtANaAl compound has
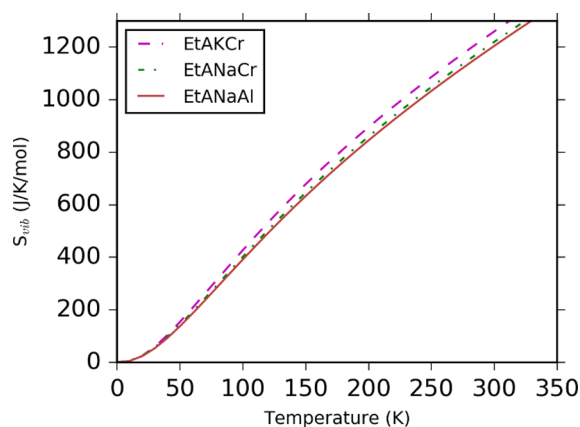

Figure 10. Vibrational entropy (S_{vib}) of the three EtA$^+$ compounds as a function of temperature. The values are per unit cell containing four molecular cations.

the lowest entropy at higher temperatures. The total vibrational entropy (S_{vib}) can be projected onto the molecular cation (S_{mol}) and the cage (S_{cage}).[43] The results given in Table 2 show that the larger entropy of the EtAKCr compound is

Table 2. Site-projected vibrational entropy (S_{vib}) at 150 K for EtA$^+$-based formate perovskites (i.e., below the transition temperatures of all materials)[a]

	EtANaCr	EtANaAl	EtAKCr
S_{vib} (J mol^{-1} K^{-1})	646	634	678
S_{mol} (J mol^{-1} K^{-1})	203	203	213
S_{cage} (J mol^{-1} K^{-1})	446	430	464

[a]S_{mol} and S_{cage} denote molecule- and cage-projected entropy.

mostly a result of a larger contribution from the cage, arising from the low frequency of the modes associated with K$^+$ cations. Finally, the structurally similar EtANaCr and EtANaAl compounds have the same entropy contribution from the molecule at 150 K, but the contribution from the cage is larger for EtANaCr, pointing out another subtle difference between the two materials.

Discussion of the Structural Properties Affecting the High-Pressure Phase Transitions. We now discuss the behavior of the MO$_6$ octahedral volume and angle distortion parameter under pressure for the EtAKCr compound and compare with the previously published EtANaCr[20] compound. Figure 4 and Figure S4a show that the volume of the KO$_6$ octahedra is strongly affected by pressure, while the volume of the CrO$_6$ octahedra is almost unchanged in the studied pressure range. In phases I–III, the volume of the KO$_6$ units shrinks by −3.26, −1.64 and −0.76 Å^3 GPa^{-1} and is reduced to 93.2% (at 0.6 GPa), 84.3% (at 2.3 GPa), and 82.1% (at 3.5 GPa) of the starting volume, respectively. The volume of CrO$_6$ octahedral units remains nearly unchanged and is equal to 99.7% (at 0.6 GPa), 97.6% (at 2.3 GPa), and 97.3% (at 3.4 GPa) of the starting volume. The corresponding rates of shrinking are equal to −0.05, −0.19, and −0.34 Å^3 GPa^{-1}, respectively. In phases I and II of the previously studied EtANaCr[20] the shrinking rate of the NaO$_6$ octahedra is slower than for the KO$_6$ units at −1.02 and −0.37 Å^3 GPa^{-1}, respectively, and causes reduction of the starting volume to 81.9% (at 3.4 GPa) and 81.2% (at 6.0 GPa). In phase I of EtANaCr the CrO$_6$ units shrink up to 3.4 GPa with the −0.11 Å^3 GPa^{-1} rate reaching 96.5% of the starting volume. In phase II, they remain unchanged within the errors of the refinement reaching 97.2% of the starting volume (at 6 GPa). It can therefore be concluded that the compressibility of the KO$_6$ octahedra is higher compared to the NaO$_6$ units, and the changes of the CrO$_6$ units are negligible in both EtANaCr and EtAKCr.

The octahedral distortion parameter (Σ) for the KO$_6$ octahedra is higher in all phases than evidenced for NaO$_6$[20] (Figure S4b). In phase I, the distortion of the KO$_6$ units decreases during compression, which was not observed for EtANaCr.[20] Upon transformation to phase II, it increases abruptly from about 65° to 145° and continues to increase during further compression (up to ca. 190° at 2.3 GPa). The transformation of the EtAKCr crystal to phase III is accompanied by a decrease of the Σ parameter to about 120°. The compression of phase III leads to a slower increase in distortion up to about 130° at the final pressure equal to 3.5 GPa. Figures 3 and 4 as well as Figure S4b show that the CrO$_6$

octahedra are almost not deformed in any of the three phases. Thus, the distortion and compression of EtAKCr are mainly governed by the KO$_6$ compression. A similar effect was observed for EtANaCr; that is, the NaO$_6$ octahedra were very susceptible to compression and were found to be responsible for the large decrease in the lattice parameters upon compression.[20]

X-ray diffraction studies on EtAKCr show that transformation between phases I, II, and III involves reorientations of the EtA$^+$ cations. In particular, the −NH$_3$$^+$ remains anchored in its ambient structure position due to strong hydrogen bonding interactions with the metal formate framework, while the −CH$_2$CH$_3$ chain is highly mobile and adaptive to the changes in pore size. Our Raman studies are consistent with this since they show very high vibrational pressure coefficients for the stretching CH modes.

Figure S5 and Tables S5 and S6 show that each hydrogen atom belonging to the amino group of the EtA$^+$ cation is bonded with the metal formate lattice by one HB with short N−O distance and an angle close to 180° as well as one longer HB with a sharper angle. In phase II they are redistributed such that one of the short bonds becomes slightly longer and one of the longer bonds becomes shorter. This pattern is very similar for one of the two independent EtA$^+$ cations in the EtANaCr phase I.[20] In phase III another rearrangement of HBs in the EtAKCr crystal takes place, where one of the long HBs become longer while the rest are found at intermediate distances. The arrangement of HBs observed in phase III is again similar to that of phase II of the previously studied EtANaCr. We suggest, therefore, that the phase transition between phases I and II for EtANaCr is similar to the phase transition between phases II and III in the EtAKCr perovskite.

The pressure-dependent Raman spectra of the EtANaAl crystal show that the substitution of Cr^{3+} ions by slightly smaller Al^{3+} ions changes its behavior under high pressure while the change in the thermal properties is very small; that is, both crystals exhibit the same type of order−disorder phase transition at almost the same temperature (369 and 373 K for EtANaAl and EtANaCr, respectively).[23] The previously reported changes in entropy (ΔS) and heat capacity associated with the temperature-induced phase transition, however, are 2 times lower for EtANaAl,[23] suggesting slightly different behavior of the occurring temperature-induced phase transitions. The low value of ΔS indicates a stronger departure from the pure order−disorder type of phase transition in EtANaAl and points to its more complex nature.[23] The DFT calculations show that the HBs in the EtANaAl compound are somewhat weaker than in the EtANaCr compound in spite of the very similar HB geometries (Table S5) and similar electronegativities of the Al^{3+} and Cr^{3+} cations (1.5 and 1.6, respectively). However, while the molecular contribution to the entropy at 150 K has the same magnitude in EtANaAl and EtANaCr (Table 2), the entropy contribution from the cage is larger for EtANaCr. This increased flexibility of the cage might outweigh the effect of the stronger hydrogen bonds, leading to the similar phase transition temperatures for the EtANaCr and EtANaAl compounds.

Overall, while the unit cell parameters and HB patterns are found to be very similar for EtANaCr and EtANaAl, the DFT calculations reveal that there are differences in the HB strength and structural flexibility of the cage as a result of the different constituent elements. These subtle differences likely give rise to the different behavior during hydrostatic compression of

EtANaCr and EtANaAl. The compression of the EtANaAl framework with weaker HBs, shorter Al—O bonds, and lower vibrational entropy allows an additional distortion of the metal formate framework that is not observed for the EtANaCr compound.

CONCLUSIONS

We have studied the structural and phonon properties of EtAKCr using high-pressure synchrotron single-crystal X-ray diffraction and Raman scattering methods and compared them with high-pressure Raman results for EtANaAl and previously obtained data for the EtANaCr crystal.

The XRD (Raman) data obtained for the EtAKCr compound show the occurrence of two high-pressure phase transitions observed at 0.75(16) GPa (1.1−1.5 GPa) and 2.4(2) GPa (2.8−3.3 GPa). Both high-pressure phases were refined in the $P2_1/n$ monoclinic symmetry and the mechanisms of the observed transitions were proposed. Initially, the increase of pressure causes a large compression of the KO_6 subnetwork along the b-axis followed by a weak decrease in its distortion. The accompanying reduction of the space available for EtA$^+$ cations forces their rearrangement leading to the change of crystal packing at 0.75(16) GPa (1.1−1.5 GPa). Upon compression of phase II, the volume of the KO_6 octahedra is reduced, accompanied by a large increase in their distortion. Finally, at 2.4(2) GPa (2.8−3.3 GPa), the second phase transition occurs and the alkyl chains of the EtA$^+$ cations change their configuration to optimize pore space requirements. This rearrangement is followed by a significant decrease in the distortion of the KO_6 units.

The high-pressure Raman scattering studies of EtANaAl revealed two structural phase transitions observed in the 1.0− 1.4 GPa range and at 4.2 GPa. The first one involves mainly the metal formate framework while the second one, similarly to the one observed for EtANaCr, leads to a large compression of the NaO_6 subnetwork and abrupt rearrangement of the EtA$^+$ cations. The DFT simulation at high pressure confirmed that the strongest compressibility of EtANaAl is expected along the b direction due to the lack of HBs in this direction.

The experimentally obtained bulk modulus as well as DFT-calculated vibrational entropy confirmed that the EtAKCr crystal is softer in comparison with the previously studied EtANaCr crystal. The calculated HB energies and vibrational entropy indicate differences between the structurally similar EtANaAl and EtANaCr compounds. The subtle interplay of these differences results in the EtANaAl crystal exhibiting an additional phase transition at lower pressures that is not observed for EtANaCr.

ASSOCIATED CONTENT

Ⓢ Supporting Information

The Supporting Information is available free of charge at https://pubs.acs.org/doi/10.1021/acs.jpcc.0c00372.

> XRD powder patterns, volume of octahedra, distortion and unit cell parameters as a function of pressure, crystal structure data, experimental and DFT calculated data of HBs, Raman data; DFT optimized structures and phonon data are available from DOI 10.5281/ zenodo.3607155 (PDF)

> Crystallographic data (CCDC 1964390-1964400) (CIF)

AUTHOR INFORMATION

Corresponding Author

Maciej Ptak − *Institute of Low Temperature and Structure Research, Polish Academy of Sciences, Wrocław, Poland;* ⓞ orcid.org/0000-0002-4639-2367; Phone: +48713954162; Email: m.ptak@intibs.pl

Authors

Katrine L. Svane − *Department of Energy Conversion and Storage, Technical University of Denmark, Kgs. Lyngby, Denmark; Department of Chemistry, University of Bath, Bath, U.K.*

Ines E. Collings − *European Synchrotron Radiation Facility, Grenoble, France; Empa - Swiss Federal Laboratories for Materials Science and Technology, Dübendorf, Switzerland*

Waldeci Paraguassu − *Faculty of Physics, Federal University of Para, Belem, Brazil;* ⓞ orcid.org/0000-0003-4980-4694

Complete contact information is available at: https://pubs.acs.org/10.1021/acs.jpcc.0c00372

Notes

The authors declare no competing financial interest.

REFERENCES

(1) Jain, P.; Ramachandran, V.; Clark, R. J.; Zhou, H. D.; Toby, B. H.; Dalal, N. S.; Kroto, H. W.; Cheetham, A. K. Multiferroic Behavior Associated with an Order−Disorder Hydrogen Bonding Transition in Metal−Organic Frameworks (MOFs) with the Perovskite ABX$_3$ Architecture. *J. Am. Chem. Soc.* **2009**, *131* (38), 13625−13627.

(2) Sanchez-Andujar, M.; Presedo, S.; Yanez-Vilar, S.; Castro-Garcia, S.; Shamir, J.; Senaris-Rodriguez, M. A. Characterization of the Order−Disorder Dielectric Transition in the Hybrid Organic− Inorganic Perovskite-Like Formate Mn(HCOO)$_3$[(CH$_3$)$_2$NH$_2$]. *Inorg. Chem.* **2010**, *49* (4), 1510−1516.

(3) Wang, W.; Yan, L.-Q.; Cong, J.-Z.; Zhao, Y.-L.; Wang, F.; Shen, S.-P.; Zou, T.; Zhang, D.; Wang, S.-G.; Han, X.-F.; et al. Magneto-electric Coupling in the Paramagnetic State of a Metal-Organic Framework. *Sci. Rep.* **2013**, *3*, 2024.

(4) Jain, P.; Stroppa, A.; Nabok, D.; Marino, A.; Rubano, A.; Paparo, D.; Matsubara, M.; Nakotte, H.; Fiebig, M.; Picozzi, S.; et al. Switchable Electric Polarization and Ferroelectric Domains in a Metal-Organic-Framework. *npj Quantum Mater.* **2016**, *1* (1), 16012.

(5) Kosa, M.; Major, D. T. Structural Trends in Hybrid Perovskites [Me$_2$NH$_2$]M[HCOO]$_3$ (M = Mn, Fe, Co, Ni, Zn): Computational Assessment Based on Bader Charge Analysis. *CrystEngComm* **2015**, *17* (2), 295−298.

(6) Duncan, H. D.; Dove, M. T.; Keen, D. A.; Phillips, A. E. Local Structure of the Metal-Organic Perovskite Dimethylammonium Manganese(II) Formate. *Dalt. Trans.* **2016**, *45* (10), 4380−4391.

(7) Gómez-Aguirre, L. C.; Pato-Doldán, B.; Mira, J.; Castro-García, S.; Senñarís-Rodríguez, M. A.; Sánchez-Andújar, M.; Singleton, J.; Zapf, V. S. Magnetic Ordering-Induced Multiferroic Behavior in [CH$_3$NH$_3$][Co(HCOO)$_3$] Metal-Organic Framework. *J. Am. Chem. Soc.* **2016**, *138* (4), 1122−1125.

(8) Zhao, T. M.; Chen, S.; Shang, R.; Wang, B. W.; Wang, Z. M.; Gao, S. Perovskite-Like Polar Lanthanide Formate Frameworks of $[NH_2NH_3][Ln(HCOO)_4]$ (Ln = Tb-Lu and Y): Synthesis, Structures, Magnetism, and Anisotropic Thermal Expansion. *Inorg. Chem.* 2016, 55 (20), 10075−10082.

(9) Liu, B.; Shang, R.; Hu, K. L.; Wang, Z. M.; Gao, S. A New Series of Chiral Metal Formate Frameworks of $[HONH_3][M^{II}(HCOO)_3]$ (M = Mn, Co, Ni, Zn, and Mg): Synthesis, Structures, and Properties. *Inorg. Chem.* 2012, 51 (24), 13363−13372.

(10) Xu, G.-C.; Ma, X.-M.; Zhang, L.; Wang, Z.-M.; Gao, S. Disorder−Order Ferroelectric Transition in the Metal Formate Framework of $[NH_4][Zn(HCOO)_3]$. *J. Am. Chem. Soc.* 2010, 132 (28), 9588−9590.

(11) Li, W.; Probert, M. R.; Kosa, M.; Bennett, T. D.; Thirumurugan, A.; Burwood, R. P.; Parinello, M.; Howard, J. A. K.; Cheetham, A. K. Negative Linear Compressibility of a Metal−Organic Framework. *J. Am. Chem. Soc.* 2012, 134 (29), 11940−11943.

(12) Zhao, J. P.; Hu, B. W.; Lloret, F.; Tao, J.; Yang, Q.; Zhang, X. F.; Bu, X. H. Magnetic Behavior Control in Niccolite Structural Metal Formate Frameworks $[NH_2(CH_3)_2][Fe^{III}M^{II}(HCOO)_6]$ (M = Fe, Mn, and Co) by Varying the Divalent Metal Ions. *Inorg. Chem.* 2010, 49 (22), 10390−10399.

(13) Li, M. Y.; Kurmoo, M.; Wang, Z. M.; Gao, S. Metal-Organic Niccolite: Synthesis, Structures, Phase Transition, and Magnetic Properties of $[CH_3NH_2(CH_2)_2NH_2CH_3][M_2(HCOO)_6]$ (M = divalent Mn, Fe, Co, Ni, Cu and Zn). *Chem. - Asian J.* 2011, 6 (11), 3084−3096.

(14) Ptak, M.; Mączka, M. M.; Gągor, A.; Sieradzki, A.; Stroppa, A.; Di Sante, D.; Perez-Mato, J. M.; Macalik, L. *Experimental and Theoretical Studies of Structural Phase Transition in a Novel Polar Perovskite-like $[C_2H_5NH_3][Na_{0.5}Fe_{0.5}(HCOO)_3]$ Formate* 2016, 45 (6), 2574−2583.

(15) Mączka, M.; Pietraszko, A.; Macalik, L.; Sieradzki, A.; Trzmiel, J.; Pikul, A. Synthesis and Order−disorder Transition in a Novel Metal Formate Framework of $[(CH_3)_2NH_2]Na_{0.5}Fe_{0.5}(HCOO)_3]$. *Dalt. Trans.* 2014, 43 (45), 17075−17084.

(16) Ptak, M.; Gagor, A.; Sieradzki, A.; Bondzior, B.; Deren, P.ła.; Ciupa, A.; Trzebiatowska, M.; Maczka, M.ła.; et al. The Effect of K+ cations on the Phase Transitions, and Structural, Dielectric and Luminescence Properties of $[Cat][K_{0.5}Cr_{0.5}(HCOO)_3]$, Where Cat Is Protonated Dimethylamine or Ethylamine. *Phys. Chem. Chem. Phys.* 2017, 19 (19), 12156−12166.

(17) Mączka, M.; Bondzior, B.; Dereń, P.; Sieradzki, A.; Trzmiel, J.; Pietraszko, A.; Hanuza, J. Synthesis and Characterization of $[(CH_3)_2NH_2][Na_{0.5}Cr_{0.5}(HCOO)_3]$: A Rare Example of Lumines- cent Metal−organic Frameworks Based on Cr(III) Ions. *Dalt. Trans.* 2015, 44 (15), 6871−6879.

(18) Ptak, M.; Svane, K. L.; Walsh, A.; Paraguassu, W. Stability and Flexibility of Heterometallic Formate Perovskites with the Dimethyl- lammonium Cation: Pressure-Induced Phase Transitions. *Phys. Chem. Chem. Phys.* 2019, 21 (8), 4200−4208.

(19) Yu, Y.; Shang, R.; Chen, S.; Wang, B.-W.; Wang, Z.-M.; Gao, S. A Series of Bimetallic AlNa Formates. *Chem. - Eur. J.* 2017, 23 (41), 9857−9871.

(20) Ptak, M.; Collings, I. E.; Svane, K. L.; Sieradzki, A.; Paraguassu, W.; Maczka, M.; Mączka, M. Pressure-Enhanced Ferroelectric Polarisation in a Polar Perovskite-like $[C_2H_5NH_3]$- $Na_{0.5}Cr_{0.5}(HCOO)_3$ Metal−organic Framework. *J. Mater. Chem. C* 2019, 7 (28), 8660−8668.

(21) Yurtseven, H.; Tarı, O. Calculation of the Thermodynamic Quantities of Perovskite Metal Organics DMAKCr and Perovskite HyFe Close to the Weakly First-Order Relaxor-like Structural Transformation Using the Mean Field Theory. *Int. J. Mod. Phys. B* 2019, 33 (11), 1−16.

(22) Plutecka, A.; Rychlewska, U. A Three-Dimensional Al^{III}/Na^I Metal-Organic Framework Resulting from Dimethyl-Formamide Hydrolysis. *Acta Crystallogr., Sect. C: Cryst. Struct. Commun.* 2009, 65 (2), 75−77.

(23) Ptak, M.; Maczka, M.; Gagor, A.; Sieradzki, A.; Bondzior, B.; Dereń, P.; Pawlus, S.; Mączka, M.; Gągor, A.; Sieradzki, A.; et al. Phase Transitions and Chromium(III) Luminescence in Perovskite- Type $[C_2H_5NH_3][Na_{0.5}Cr_xAl_{0.5-x}(HCOO)_3]$ (x = 0, 0.025, 0.5), Correlated with Structural, Dielectric and Phonon Properties. *Phys. Chem. Chem. Phys.* 2016, 18 (42), 29629−29640.

(24) Collings, I. E.; Bykov, M.; Bykova, E.; Tucker, M. G.; Petitgirard, S.; Hanfland, M.; Glazyrin, K.; van Smaalen, S.; Goodwin, A. L.; Dubrovinsky, L.; et al. Structural Distortions in the High- Pressure Polar Phases of Ammonium Metal Formates. *CrystEngComm* 2016, 18 (46), 8849−8857.

(25) Collings, I. E.; Manna, R. S.; Tsirlin, A. A.; Bykov, M.; Bykova, E.; Hanfland, M.; Gegenwart, P.; Van Smaalen, S.; Dubrovinsky, L.; Dubrovinskaia, N. Pressure Dependence of Spin Canting in Ammonium Metal Formate Antiferromagnets. *Phys. Chem. Chem. Phys.* 2018, 20 (37), 24465−24476.

(26) Yang, Z.; Cai, G.; Bull, C. L.; Tucker, M. G.; Dove, M. T.; Friedrich, A.; Phillips, A. E. Hydrogen-Bond-Mediated Structural Variation of Metal Guanidinium Formate Hybrid Perovskites under Pressure. *Philos. Trans. R. Soc., A* 2019, 377 (2149), 20180227.

(27) Sobczak, S.; Katrusiak, A. Environment-Controlled Postsyn- thetic Modifications of Iron Formate Frameworks. *Inorg. Chem.* 2019, 58 (17), 11773−11781.

(28) Chitnis, A. V.; Bhatt, H.; Maczka, M.; Deo, M. N.; Garg, N. Remarkable Resilience of the Formate Cage in a Multiferroic Metal Organic Framework Material: Dimethyl Ammonium Manganese Formate (DMAMnF). *Dalt. Trans.* 2018, 47 (37), 12993−13005.

(29) Sobczak, S.; Chitnis, A.; Andrzejewski, M.; Maczka, M.; Gohil, S.; Garg, N.; Katrusiak, A. Framework and Coordination Strain in Two Isostructural Hybrid Metal-Organic Perovskites. *CrystEngComm* 2018, 20 (36), 5348−5355.

(30) Mączka, M.; Kadłubański, P.; Freire, P. T. C.; Macalik, B.; Paraguassu, W.; Hermanowicz, K.; Hanuza, J. Temperature- and Pressure-Induced Phase Transitions in the Metal Formate Framework of $[ND_4][Zn(DCOO)_3]$ and $[NH_4][Zn(HCOO)_3]$. *Inorg. Chem.* 2014, 53 (18), 9615−9624.

(31) Mączka, M.; Marinho Costa, N. L.; Gągor, A.; Paraguassu, W.; Sieradzki, A.; Hanuza, J. *Phys. Chem. Chem. Phys.* 2016, 18 (20), 13993−14000.

(32) Mączka, M.; Gągor, A.; Ptak, M.; Paraguassu, W.; Da Silva, T. A.; Sieradzki, A.; Pikul, A. Phase Transitions and Coexistence of Magnetic and Electric Orders in the Methylhydrazinium Metal Formate Frameworks. *Chem. Mater.* 2017, 29 (5), 2264−2275.

(33) Viswanathan, M. High-Pressure Phase Transitions with Group−subgroup Disagreement in Metal Guanidinium Formates. *CrystEngComm* 2018, 20 (43), 6861−6866.

(34) Li, W.; Thirumurugan, A.; Barton, P. T.; Lin, Z.; Henke, S.; Yeung, H. H.-M.; Wharmby, M. T.; Bithell, E. G.; Howard, C. J.; Cheetham, A. K. Mechanical Tunability via Hydrogen Bonding in Metal−Organic Frameworks with the Perovskite Architecture. *J. Am. Chem. Soc.* 2014, 136 (22), 7801−7804.

(35) MącZka, M.; Almeida da Silva, T.; Paraguassu, W.; Pereira Da Silva, K. Raman Scattering Studies of Pressure-Induced Phase Transitions in Perovskite Formates $[(CH_3)_2NH_2][Mg(HCOO)_3]$ and $[(CH_3)_2NH_2][Cd(HCOO)_3]$. *Spectrochim. Acta, Part A* 2016, 156, 112−117.

(36) Collings, I. E.; Bykov, M.; Bykova, E.; Hanfland, M.; Van Smaalen, S.; Dubrovinsky, L.; Dubrovinskaia, N. Disorder-Order Transitions in the Perovskite Metal-Organic Frameworks $[(CH_3)_2NH_2][M(HCOO)_3]$ at High Pressure. *CrystEngComm* 2018, 20 (25), 3512−3521.

(37) Rigaku Oxford Diffraction CrysAlisPro Software System, Version 1.171, Rigaku. 2015.

(38) Kresse, G.; Hafner, J. Ab Initio Molecular Dynamics for Liquid Metals. *Phys. Rev. B: Condens. Matter Mater. Phys.* 1993, 47 (1), 558−561.

(39) Perdew, J. P.; Ruzsinszky, A.; Csonka, G. I.; Vydrov, O. A.; Scuseria, G. E.; Constantin, L. A.; Zhou, X.; Burke, K. Restoring the

Density-Gradient Expansion for Exchange in Solids and Surfaces. *Phys. Rev. Lett.* **2008**, *100* (13), 136406.

(40) Grimme, S.; Antony, J.; Ehrlich, S.; Krieg, H. A Consistent and Accurate *Ab Initio* Parametrization of Density Functional Dispersion Correction (DFT-D) for the 94 Elements H-Pu. *J. Chem. Phys.* **2010**, *132* (15), 154104.

(41) Grimme, S.; Ehrlich, S.; Goerigk, L. Effect of the Damping Function in Dispersion Corrected Density Functional Theory. *J. Comput. Chem.* **2011**, *32* (7), 1456−1465.

(42) Togo, A.; Tanaka, I. First Principles Phonon Calculations in Materials Science. *Scr. Mater.* **2015**, *108*, 1−5.

(43) Butler, K. T.; Svane, K.; Kieslich, G.; Cheetham, A. K.; Walsh, A. Microscopic Origin of Entropy-Driven Polymorphism in Hybrid Organic-Inorganic Perovskite Materials. *Phys. Rev. B: Condens. Matter Mater. Phys.* **2016**, *94* (18), 180103.

(44) Svane, K. L.; Forse, A. C.; Grey, C. P.; Kieslich, G.; Cheetham, A. K.; Walsh, A.; Butler, K. T. How Strong Is the Hydrogen Bond in Hybrid Perovskites? *J. Phys. Chem. Lett.* **2017**, *8* (24), 6154−6159.

(45) Cliffe, M. J.; Goodwin, A. L. IUCr. *PASCal*: A Principal Axis Strain Calculator for Thermal Expansion and Compressibility Determination. *J. Appl. Crystallogr.* **2012**, *45* (6), 1321−1329.

(46) Angel, R. J.; Alvaro, M.; Gonzalez-Platas, J. EosFit7c and a Fortran Module (Library) for Equation of State Calculations. *Z. Kristallogr. - Cryst. Mater.* **2014**, *229* (5), 405−419.

(47) Shannon, R. D. Revised Effective Ionic Radii and Systematic Studies of Interatomie Distances in Halides and Chaleogenides. *Acta Crystallogr., Sect. A: Cryst. Phys., Diffr., Theor. Gen. Crystallogr.* **1976**, *32*, 751−767.

(48) Guionneau, P.; Marchivie, M.; Bravic, G.; Létard, J.-F.; Chasseau, D. *Structural Aspects of Spin Crossover. Example of the [Fe^{II}Ln(NCS)_2] Complexes*; Springer: Berlin, pp 97−128.

(49) Kieslich, G.; Sun, S.; Cheetham, A. K. Solid-State Principles Applied to Organic−inorganic Perovskites: New Tricks for an Old Dog. *Chem. Sci.* **2014**, *5* (12), 4712−4715.

(50) Wang, Z.; Zhang, B.; Otsuka, T.; Inoue, K.; Kobayashi, H.; Kurmoo, M. Anionic NaCl-Type Frameworks of $[Mn^{II}(HCOO)_3^-]$, Templated by Alkylammonium, Exhibit Weak Ferromagnetism. *Dalt. Trans.* **2004**, 2209−2216.

(51) Kieslich, G.; Kumagai, S.; Butler, K. T.; Okamura, T.; Hendon, C. H.; Sun, S.; Yamashita, M.; Walsh, A.; Cheetham, A. K. Role of Entropic Effects in Controlling the Polymorphism in Formate ABX_3 Metal-Organic Frameworks. *Chem. Commun.* **2015**, *51* (85), 15538−15541.

(52) Kieslich, G.; Skelton, J. M.; Armstrong, J.; Wu, Y.; Wei, F.; Svane, K. L.; Walsh, A.; Butler, K. T. Hydrogen Bonding versus Entropy: Revealing the Underlying Thermodynamics of the Hybrid Organic-Inorganic Perovskite $[CH_3NH_3]PbBr_3$. *Chem. Mater.* **2018**, *30* (24), 8782−8788.